TU Delft

Delft University of Technology

Sources of Image Degradation and their Correction in Single-sided Ultrasound Imaging of Heterogeneous Tissues

Renaud, Guillaume; Soulioti, Danai E.; Pinton, Gianmarco

DOI
10.1002/9781394306626.ch8

Publication date
2024

Document Version
Final published version

Published in
Innovative Ultrasound Imaging Techniques

Citation (APA)
Renaud, G., Soulioti, D. E., & Pinton, G. (2024). Sources of Image Degradation and their Correction in Single-sided Ultrasound Imaging of Heterogeneous Tissues. In *Innovative Ultrasound Imaging Techniques: Biomedical Applications* (pp. 249-283). Wiley. https://doi.org/10.1002/9781394306626.ch8

Important note
To cite this publication, please use the final published version (if applicable).
Please check the document version above.

Copyright
Other than for strictly personal use, it is not permitted to download, forward or distribute the text or part of it, without the consent of the author(s) and/or copyright holder(s), unless the work is under an open content license such as Creative Commons.

Takedown policy
Please contact us and provide details if you believe this document breaches copyrights.
We will remove access to the work immediately and investigate your claim.

This work is downloaded from Delft University of Technology.
For technical reasons the number of authors shown on this cover page is limited to a maximum of 10.

Green Open Access added to TU Delft Institutional Repository

'You share, we take care!' - Taverne project

https://www.openaccess.nl/en/you-share-we-take-care

Otherwise as indicated in the copyright section: the publisher is the copyright holder of this work and the author uses the Dutch legislation to make this work public.

8

Sources of image degradation and their correction in single-sided ultrasound imaging of heterogeneous tissues

Guillaume Renaud (Department of Imaging Physics, Delft University of Technology, The Netherlands, g.g.j.renaud@tudelft.nl)
& Danai E Soulioti (Joint Dept. of Biomedical Engineering, University of North Carolina at Chapel Hill and North Carolina State University, USA, soulioti@email.unc.edu)
& Gianmarco Pinton (Joint Dept. of Biomedical Engineering, University of North Carolina at Chapel Hill and North Carolina State University, USA, gia@email.unc.edu)

Contents

8.1. Introduction

The generation of an ultrasound image, or echography, is based on determining the time it takes for a wave to propagate from a ultrasound transducer to a target (forward propagation) and the time for the resulting echo to return to the probe (backward propagation). Approaches for image reconstruction rely on assumptions of wave propagation in the region of interest that convert the travel time from the transducer to a target and from a target to the transducer into spatial maps or images from the echoes. These simplifying assumptions can be divided into three categories:

1) Uniformity of the wave speed
2) Uniformity of attenuation
3) Absence of multiple scattering

Even though complex heterogeneous media, such as the soft tissue in the human body, clearly violate these assumptions, ultrasound scanners are capable of producing exquisite images. Obtaining high quality images depends on approaches that are either insensitive to these sources of image degradation or are capable of correcting them.

With the continuous improvement of the quality of electronics, transducer sensitivity and image processing for optimizing display, the flaws in ultrasound images resulting from simplifying assumptions made during image reconstruction become more and more noticeable. The development over the past 20 years to software-based image reconstruction and large bandwidth, high frame-rate imaging hardware has enabled new imaging approaches (e.g. imaging of tissue stiffness with shear-wave elastography, ultrafast imaging of blood flow) and has greatly improved the versatility of ultrasound imaging. Sophisticated image sequence design, such as synthetically-focused ultrasound imaging which stores digitized raw echo signals in computer memory and utilizes unfocused transmit beams instead of focused transmit beams, is straightforward to implement in a modern scanner. By lowering these technological barriers there is a renewed focus on understanding and overcoming the underlying physical sources of image degradation that occur from the wave propagation physics and how it applies to the wide variety of image formation approaches.

Understanding and accounting for these physical sources of degradation remains a critical challenge in many applications of ultrasound imaging. Transcranial imaging,

for example, remains a highly challenging environment for ultrasound imaging due to strong acoustical barrier presented by the skull. Even in transabominal imaging, a significant portion of patients are difficult to image due to thick layers of subcutaneous fat which obscure the underlying anatomy.

The potential offered due to the greater performance and the increased versatility of ultrasound provides new arms with which to combat effects such as aberration or reverberation that can degrade ultrasound images. The objective of this chapter is to review the current state of knowledge on physical sources of image degradation within the medium and give possible future research directions to further improve image quality in medical ultrasound imaging. The architecture and performances of modern ultrasound systems provide us with a versatile technology that can be used to revisit pioneering work, improve it and perhaps even go far beyond it.

8.2. Sources of image degradation

Among all sources of image degradation, side lobes and grating lobes are well known. Their origin pertains to the finite size of the transducer aperture and the periodicity of the transducer array, respectively. Because their cause is not the heterogeneity of the scanned region, this issue will not be addressed in this book chapter. For detailed information about the origin of side lobes and grating lobes and solutions to reduce them, we refer the readers to (Shung 2015 ; Szabo 2013). This book chapter concentrates on the sources of image degradation arising from the heterogeneity of the scanned region.

The focus will also be on conventional i.e. single-sided ultrasound imaging, which relies on:

1) The transmission of a set of pulsed ultrasound beams in the region of interest with an array transducer;

2) The recording (for each transmission) of ultrasound waves scattered by heterogeneities in the region of interest, typically with the same array transducer;

3) The use of an algorithm for image reconstruction that processes the recorded scattered echo signals.

Tissue inhomogeneities create a variety of image artefacts. Some of them, in particular the edge shadowing artefact, the mirror-image artefact and the comet tail artefact, have been well described in the literature (see for instance chapter 5 in (Hoskins *et al*. 2019)) and therefore will not be treated in this book chapter.

8.2.1. *Aberration and aberrators*

8.2.1.1. *Definitions*

An aberration refers to a defect in the ultrasound image that is caused by an inaccurate description of ultrasound propagation. An aberrator refers to any subregion in the scanned region of interest that causes an aberration. An aberrator typically engenders ultrasound wave phenomena that are more complex than the physics modeled in the algorithm for image reconstruction.
Aberrations are often studied in terms of amplitude aberration and phase aberration. Amplitude aberration refers to a departure of the performance of the ultrasound imaging system caused by an altered amplitude (compared to amplitude expected with the three major assumptions) of recorded ultrasound wavelets. Phase aberration refers to a departure of the performance of the ultrasound imaging system caused by the altered arrival time (or phase) of recorded ultrasound wavelets.

8.2.1.2. *Aberration in weakly and highly heterogeneous regions*

The wave speed in the region between the ultrasound transducer and the region of interest is always unknown in medical ultrasound imaging. Fortunately, the range of variation of the ultrasound wave speed in biological soft tissues is well known (1400-1700 m/s). An ultrasound scanner typically uses a constant value of 1540 m/s during image reconstruction because this value is generally accepted as the average speed of sound in biological soft tissues. However, the actual average wave speed in the scanned region never equals 1540 m/s. Even if the scanned region is weakly heterogeneous, using an incorrect average wave speed during image reconstruction leads to phase aberration, which leads to sub-optimal image reconstruction.

The situation becomes far more complicated if the scanned region is highly heterogeneous. The sub-region with the most atypical properties would be called the aberrator. It can be a layer (for instance a fat layer under the skin or the bone layer of the skull) or a circumscribed area (for instance a fat inclusion in breast or a cyst). Two tissue types are responsible for most severe aberrations:

– fat, which has a low wave speed and a low mass density (1400 m/s and 900 kg/m^3, respectively)

– bone, which has a high wave speed and a high mass density (1600-4200 m/s and 1100-2000 kg/m^3, exact values are highly dependent on porosity)

Typical situations where strong aberration can occur are:

– ultrasound imaging of organs in the abdomen due to adipose tissue beneath the skin (subcutaneous fat) and around organs (visceral fat)

– breast ultrasound imaging because breast tissue contains a large amount of adipose tissue (subcutaneous fat)

– transcranial ultrasound imaging of the brain due to the skull

– intraosseous ultrasound imaging

8.2.1.3. *Phase aberration: orders of magnitude and characterization*

An extended plane or spherical wavefront propagates in a homogeneous, non-attenuating medium without local distortion of its phase or amplitude. However, when propagating through a few centimeters of heterogeneous biological tissue, an extended wavefront experiences local distortion of its phase because its travels across regions with different wave speeds.

Figure 8.1 illustrates these effects with synthetic data generated numerically by propagating in a two-dimensional space the wavefront emitted by a point source located in the medium and received by a transducer array (128 elements, pitch equals 0.3 mm, center ultrasond frequency equals 5 MHz). This is equivalent to studying only the return trip of backscattered echoes (from targets to the transducer array) during pulse-echo ultrasound imaging. The aberration caused by a model of abdominal wall tissue is simulated.

A wavefront scattered by a target and recorded by a transducer array contains a geometric delay component that has a curvature large compared to the fluctuations caused by tissue heterogeneities. After geometric correction of the recorded wavefront, it is possible to extract the arrival time fluctuations caused by tissue heterogeneities, *i.e.* phase aberration (panels e) and f) in Figure 8.1).

Several research groups (Freiburger *et al*. 1992 ; Trahey *et al*. 1991 ; Sumino and Waag 1991 ; Liu and Waag 1995) have proposed to characterize the phase aberration by measuring the amplitude of the arrival time fluctuations and the spatial variation of wavefront distortion in the array aperture. The amplitude of the arrival time fluctuations is measured with the root-mean-square (rms) value which characterizes the strength of the phase aberration. The spatial variation of wavefront distortion in the array aperture is measured with a correlation length defined as the full width half-maximum of the autocorrelation function (in space) of the arrival time fluctuations, which characterizes the complexity of the phase aberration. It is possible to correct for the phase aberration (Section 8.3.2) only if the transducer array can properly sample the spatial variation of the wavefront distortion. More specifically the spatial period in the transducer array (pitch) must be smaller than the spatial correlation length of the aberration profile.

In the case shown in Figure 8.1, the rms value of the arrival time fluctuations is 56 ns and the spatial correlation length of the aberration profile is 4 mm. It is also worth noticing that there exists an offset error in the arrival times with the abdominal wall, since all arrival times are larger than that expected in a uniform medium with a sound speed of 1540 m/s. This means that the average sound speed in the abdominal wall model is slightly less than 1540 m/s.

Experimental studies have reported arrival time fluctuations up to 100 ns as an ultrasound wave propagates through a 2cm-thick layer of abdominal wall or breast

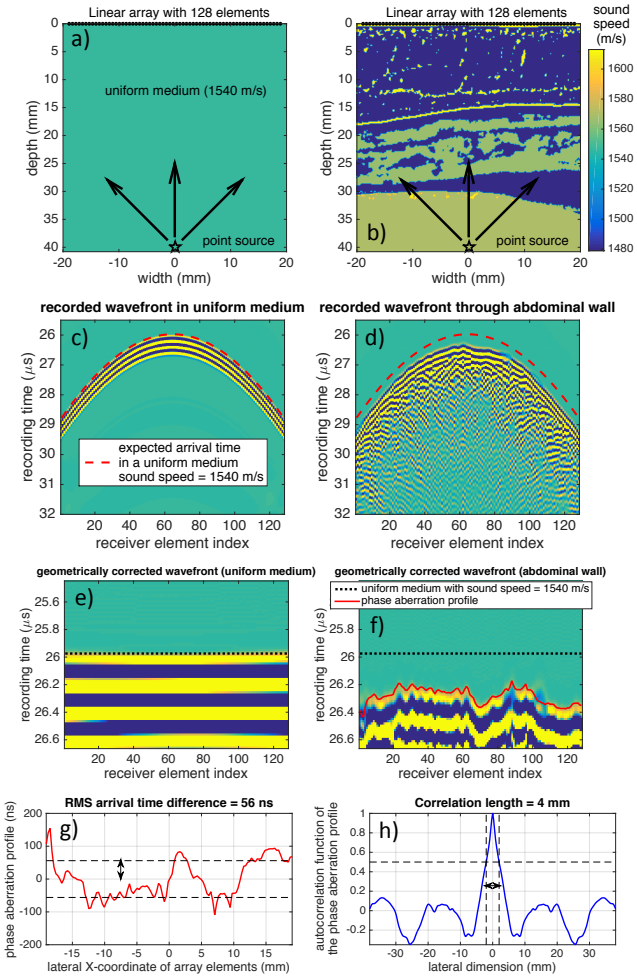

Figure 8.1 – Illustration of phase aberration during the return trip only (simulating backscattering from a point target is analog to placing a point source in the medium). Synthetic signals were generated with a time-domain wave propagation solver through a) a uniform medium and b) an abdominal wall model. The wavefronts recorded by a transducer array are shown in panels c) and d). After geometric correction, the wavefront is perfectly flat in the uniform medium (panel e) while arrival time fluctuations remain as a result of phase aberration caused by the abdominal wall (panel f). The phase aberration profile is characterized by rms value of the arrival time fluctuations (panel g) and the spatial correlation length (panel h).

(Abdominal/Body Wall: (Hinkelman *et al*. 1994 ; O'Donnell and Flax 1988*b* ; Sumino and Waag 1991), Breast: (Trahey *et al*. 1991 ; Hinkelman *et al*. 1995)), with a root mean square value over the transducer aperture in the range 30-70 ns. The skull generates larger phase aberrations, up to 1 μs where the skull is the thickest (Marsac *et al*. 2017 ; Marquet *et al*. 2009). For diagnostic ultrasound, the temporal region of the skull is often used because it is thinner and the root mean square phase aberration over the transducer aperture is in the range of 50-150 ns for this region (Lindsey and Smith 2013 ; Phillips *et al*. 1975*b* ; Tanter *et al*. 1998 ; Soulioti *et al*. 2020).
The correlation length measured for the abdominal wall or the breast was reported between 3 and 11 mm (Hinkelman *et al*. 1994 ; Freiburger *et al*. 1992). For the temporal bone of the skull, the correlation length was measured between 1 and 4 mm (Lindsey and Smith 2013 ; Vignon *et al*. 2008).
Thus, the phase aberration is most often stronger when imaging through the temporal bone of the skull than when imaging the breast or through the abdominal wall.

8.2.1.4. *Consequences of phase aberration on beam focusing, beam steering, and image reconstruction*

It has been shown that the quality of *in vivo* liver scans is degraded when phase aberrations are strong (O'Donnell and Flax 1988*b*).
Traditional ultrasound imaging relies on the transmission of focused ultrasound beams. Beam focusing and steering is generated by delaying the emission of individual elements of the transducer array. The specific transmit delays are calculated such that all wavelets emitted by individual elements arrive at the same instant at the desired focal point. The accurate calculation of these transmit delays requires knowing the wave speed in the scanned area. Current medical ultrasound scanners assume a uniform wave speed of 1540 m/s when calculating transmit delays. In the presence of strong aberrators (fat or bone), the calculation of transmit delays is obviously erroneous and leads to sub-optimal beam focusing and steering and hence poor image quality.
Phase aberration also has an important impact on image reconstruction. The most widely used algorithm for image reconstruction is delay-and-sum. Each image pixel is considered as a hypothetical scattering point. The reconstruction algorithm operates as a summation over the receive aperture of the transducer array of the recorded echo signals evaluated at the calculated round-trip travel times (see Chapter 2 of this book). For each image pixel, the calculated round-trip travel times is the sum of the forward travel time (from the transducer to the image pixel) and the return travel times (from the image pixel to each individual element of the transducer array). Current medical ultrasound scanners assume a uniform wave speed of 1540 m/s to calculate the forward travel time and return travel times. As for transmit delays, in the presence of strong aberrators (fat or bone), the calculation of the forward travel time and return travel times is obviously incorrect and leads to sub-optimal image reconstruction.

8.2.1.5. *Amplitude aberration*

In addition to arrival time fluctuations (phase aberration), amplitude fluctuations are observed in a wavefront that traveled through heterogeneous tissue. They are created by the spatial variation of ultrasonic attenuation magnitude because different tissue types have different attenuation strength. These amplitude fluctuations are also due to refraction and diffraction by tissue heterogeneities, which results in constructive or destructive phase interferences.
Experimental studies in soft tissues (through a 2cm-thick abdominal wall) reported small amplitude aberration (about 2-4 dB, (Hinkelman *et al*. 1994 ; O'Donnell and Flax 1988*b*)). In contrast, the skull can produce large amplitude aberrations of up to 20 dB (Tanter *et al*. 1998).
However, in recent work it was shown that the correction of amplitude aberration results in small improvement of image quality (Soulioti *et al*. 2020) compared to the correction of phase aberration. Most work in literature is indeed focused on the correction of phase aberration. For this reason, this book chapter will not discuss methods for the correction of amplitude aberration.

8.2.2. *Multiple scattering (reverberation)*

Wave speed and mass density heterogeneities can cause multiple scattering (or reverberation). In fact, aberrations and multiple scattering share the same cause, and they most often coexist. Multiple scattering is typically ignored during image reconstruction. Indeed, traditional image reconstruction assumes that echo signals are generated by a single interaction between the ultrasound pulse transmitted by a probe and scatterers in the medium. As a result, echoes arising from multiply scattered waves appear as clutter in the ultrasound image. A region made of multiple layers of different tissue types is often favorable to the generation of multiple scattering.

In a heterogeneous medium comprising various interfaces with large impedance mismatches, such as between fat and muscle, strong reflections might occur. Media with a layered structure, such as connective tissue, tend to trap acoustic energy, causing it to reverberate between layers. A portion of the trapped energy is transmitted back to the ultrasonic transducer, where it overlays acoustic noise onto its received signals.

When the tissue layers are nearly normal to the direction of wave propagation, the noise is visible in the ultrasonic image as bright bands that occur at integer multiples of the spatial period, or thickness, of the tissue layers. If the layers are not normal to the direction of propagation, the resulting reverberation is less coherent and appears as a haze overlaid on the B-mode (Brightness-mode) image. This behaviour would be expected in higher body-mass index patients where there are many connective tissue layer boundaries within the increased thickness of fat tissue (Pinton *et al*. 2011).

8.2.3. *Importance of the ultrasound frequency*

In general, the highest ultrasound frequency is desired to achieve the best spatial resolution in the ultrasound image. However ultrasound attenuation increases with the ultrasound frequency. As a result, superficial imaging can use rather high frequencies (up to 15 MHz) while deep imaging is restricted to lower frequencies (close to 3 MHz). Besides the challenge of attenuation, increasing the ultrasound frequency may also further degrade image quality in heterogeneous tissues. While arrival time fluctuations are measured in nano- or micro-seconds, the impact of the phase aberration on image degradation depends on the ultrasound frequency. The magnitude of the phase aberration can also be expressed in radians or as a fraction of an ultrasound temporal period. Phase aberration causing arrival time fluctuations of T/10 or less, where T is the temporal period of the ultrasound wave, does not result in significant image degradation. Thus imaging with a low ultrasound frequency is less impacted by phase aberration than imaging with a higher ultrasound frequency.
The ultrasound frequency also determines the magnitude of single and multiple diffuse scattering, *i.e.* scattering by small inhomogeneities. Indeed diffuse scattering increases with the ultrasound frequency, particularly if the ultrasound wavelength becomes close to the mean size of the small inhomogeneities. For example, in transcranial imaging at 3 MHz, the ultrasound wavelength is close to 1 mm in cortical bone and the mean pore diameter in cortical bone was reported close to 90 μm in human skulls (Alexander *et al*. 2019). This means that the inhomogeneities in the dense bone tissue type of the skull are 10 times smaller than the wavelength. Using a higher ultrasound frequency for transcranial imaging would likely lead to enhanced clutter in the image due to enhanced multiple diffuse scattering.

8.2.4. *Illustration of the impact of aberration and multiple scattering on image quality with numerical simulations*

It is common practice to evaluate the performance of an imaging system using the point spread function (PSF), *i.e.* the spatial impulse response of the imaging system. The PSF is obtained by producing a B-mode (Brightness-mode) image of a point target (sub-wavelength object). The PSF can be described as:

– a main central component, which determines axial and lateral spatial resolution in the ultrasound image, and

– secondary components expanding from the main component with smaller amplitude, which determine contrast resolution in the ultrasound image.

Image quality is optimal if the spatial extent of the main central component is as small as possible and if the amplitude of secondary components is as weak as possible.

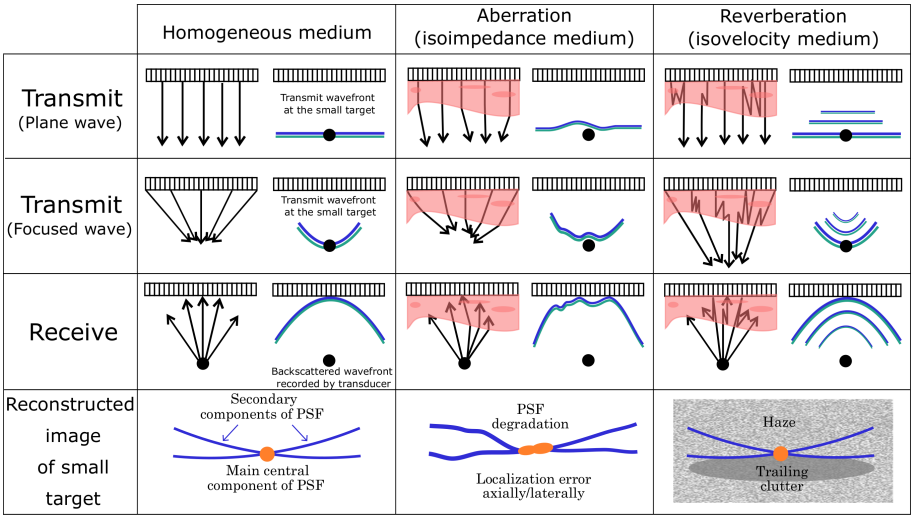

Figure 8.2 – Schematic representation of wave propagation in a homogeneous, isoimpedance and isovelocity medium. Two different transmit schemes, plane wave and focused wave are shown. The transmit wavefront reaching the point target and the wavefront received at the transducer array are depicted for all cases. The reconstructed image of the small target in different media is shown in the bottom row.

A schematic of typical PSFs in different media as well as transmit and receive wavefronts for a plane or focused transmit beam are shown in Fig. 8.2. In a homogeneous medium (left column) the wave is transmitted and received by the transducer without any disturbance thus an ideal PSF is produced. If we consider a hypothetical medium where aberration is present, but multiple scattering is absent (isoimpedance medium), the effects in the middle column are seen. Refraction causes distortion of the wavefront on transmit and receive, thus the final PSF is degraded in shape and size and might also present registration errors in both directions. Lastly, when multiple scattering is present, but sound speed inhomogeneity is artificially absent (isovelocity medium), the PSF is no longer distorted in shape, however a hazing effect is introduced due to multipath reverberations caused by reflections of the pulse at different medium layers (right column). Some portion of the energy is reflected towards the transducer, but a portion is also reflected towards the point target, causing the transmit waveform to become elongated, which causes trailing clutter to appear behind the main component of the PSF.

Figure 8.3 illustrates transabdominal sound speed maps and B-mode images simulated using the Fullwave (Pinton, Dahl, Rosenzweig and Trahey 2009) numerical solver for a curved transducer at 3.7 MHz. Fig. 8.3A is the input sound

speed map used in the simulation which is segmented from the Visible Human Project optical dataset (`https://www.nlm.nih.gov/research/visible/visible_human.html`) and processed by assigning tabulated values to known structures such as fat, muscle and connective tissue. To simulate compression typically exerted by the sonographer during abdominal imaging, an arc following the shape of the transducer has been introduced to the maps. To accurately simulate tissue response, random scatterers are placed throughout the abdomen. Figures 8.3B-E, all use a 3.7 MHz, 2 cycle single transmit emission focused at the depth of a point target, marked in red in Fig. 8.3A. Image reconstruction is performed using a conventional delay-and-sum algorithm. Fig. 8.3B, shows an emission in a homogeneous medium, while Fig. 8.3C shows the same target through the abdominal wall. The effects of aberration can be seen on the target. Reverberation has a more localized effect, mainly affecting the first 40 mm of the B-mode image. In Fig. 8.3D, in order to remove phase aberration, the sound speed maps of the abdominal wall are set to be constant, while the density maps remain unchanged. This results in an isovelocity B-mode image showing the effects of reverberation. To obtain an isoimpedance B-mode image, where the effects of reverberation are diminished, we performed a linear subtraction of the image obtained with an additional simulation through the abdominal wall but without the target (not shown) from the image shown in Fig. 8.3C. This results in Fig. 8.3E, where multiple reverberations except trailing clutter are removed, but the effects of aberration are still intact.

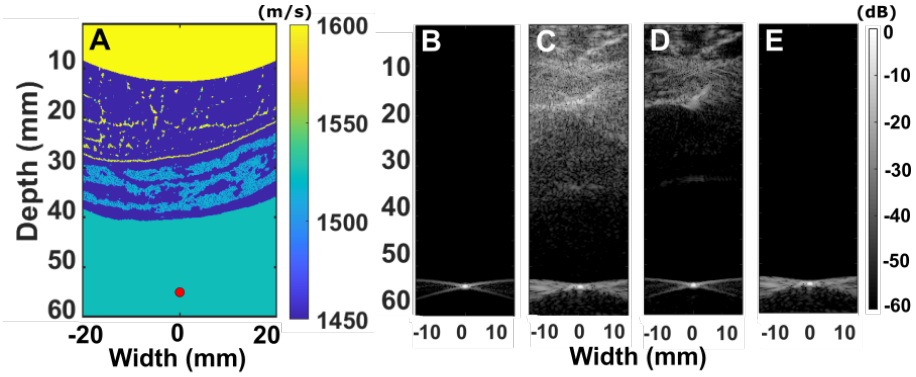

Figure 8.3 – A, Speed of sound map for the human abdominal wall. B-E, B-mode images for a target 55 mm from the transducer normalized by the maximum amplitude of the homogeneous case. The transducer was apodized at half the aperture. B is the B-mode image obtained through a homogeneous medium. C is the B-mode image obtained through the heterogeneous abdominal wall. D is the isovelocity B-mode image. E is the isoimpedance B-mode image obtained through clutter subtraction.

A very similar process as described for Figure 8.3 was used in generating Figure 8.4. A human skull was scanned with x-ray Computed Tomography and then converted to speed of sound, density and attenuation maps through a linear Hounsfield to density transformation (Lagravere *et al*. 2006). Fig. 8.4A shows the sound speed map used in the Fullwave simulations. A point target was placed at 50 mm and a full-aperture, single transmit focused emission was used. The transmit frequency in this case is 2.5 MHz. As described before, homogeneous (Fig. 8.4B), heterogeneous (Fig. 8.4C), isovelocity (Fig. 8.4D) and isoimpedance (Fig. 8.4E) B-modes images show the effects of aberration and reverberation collectively and separately. In transcranial imaging, aberration is a well known and extensively characterized as a source of image distortion. Reverberation also degrades image quality, it reduces the target amplitude and compromises spatial resolution. Reverberation effects are more pronounced at shallower depths, but their contribution persists even at depths larger than 6 cm, as shown in Fig. 8.4C.

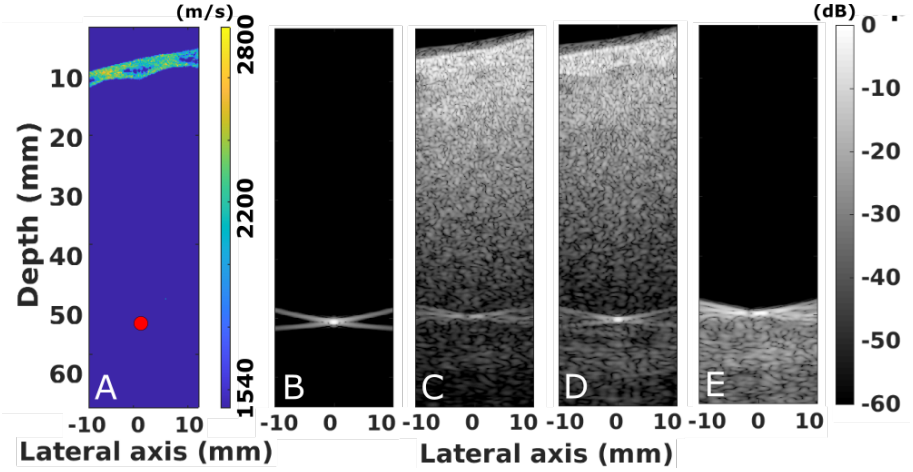

Figure 8.4 – A, Speed of sound map for a CT-derived human skull slice. B-E, B-mode images for a target at 50 mm from the transducer normalized by the maximum amplitude of the homogeneous case. B, is the homogeneous B-mode, C is the heterogeneous B-mode through the skull, D is the isovelocity B-mode. E is the isoimpedance B-mode obtained through clutter subtraction.

To illustrate the depth dependency of reverberation and its effect on image quality a point target was placed at 3 different depths, namely 30, 50 and 70 mm, for the same map shown in Fig. 8.5A. At the shallow depth in Fig. 8.5B, reverberation completely compromises the target, whereas at 70 mm Fig. 8.5D, aberration is practically the sole degrading mechanism. At 50 mm, both mechanisms appear to contribute to the degradation. Trailing clutter is the result of the pulse lengthening with propagation and is independent of depth, thus it persists in all cases.

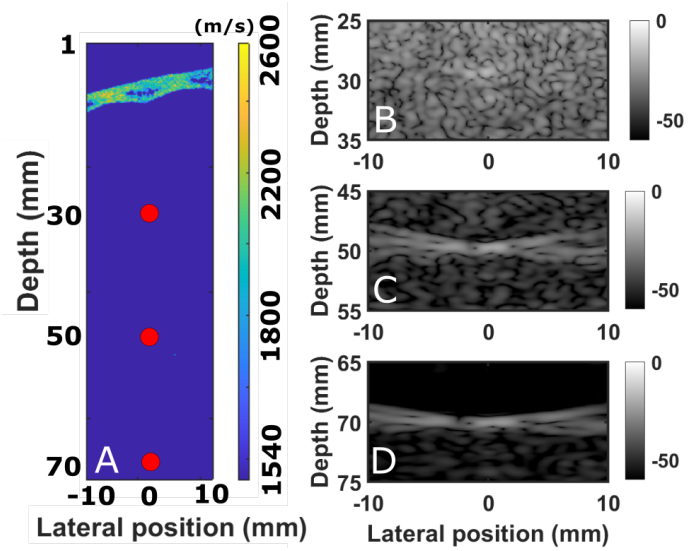

Figure 8.5 – A, illustration of sound speed maps for imaging point targets through the human skull at three different depths, namely: B, at 3 cm, C, at 5 cm and D, at 7 cm. No aberration correction has been applied. Gray scale units are in normalized dB.

8.2.5. *Anisotropic elasticity in bone*

Ultrasound imaging of structures within bones or behind bones is very challenging, in particular because of the large wave speed difference between mineralized bone tissue and soft tissues. In addition to this, the elasticity of bone tissue is anisotropic, which results in wave speed anisotropy. The least porous type of bone tissue, called compact or cortical bone, has been the most studied (Yoon and Lawrence Katz 1976 ; Ashman *et al*. 1984 ; Peterson and Dechow 2003 ; Granke *et al*. 2011). The anisotropic elasticity of cortical bone is well approximated by a model of transverse isotropy. For the diaphysis of a long bone, the symmetry axis is nearly aligned with the bone axis (Figure 8.6), it corresponds to the direction of maximum compressional wave speed. In any direction normal to the symmetry axis, the compressional wave speed is about 20% smaller. Transcranial ultrasound imaging is performed through the squamous part of the temporal bone of the skull, which is often a single layer of cortical bone. The elasticity of this region of the temporal bone can be approximated with transverse isotropy, however the symmetry axis (which corresponds to the direction of maximum compressional wave speed) was shown to be inconsistent among specimens (Peterson and Dechow 2003).

In a medium with elastic anisotropy, the wave speed is described by two parameters, the phase velocity and the group velocity. A compressional wave has a quasi longitudinal polarization and its phase velocity v_P is determined by four parameters α_0, β_0,

ε and δ^* (Thomsen 1986):

$$v_P(\theta) = \alpha_0 \left[1 + \varepsilon \cos^2(\theta) + D^* \Big(\theta, \alpha_0, \beta_0, \varepsilon, \delta^* \Big) \right]^{1/2} \quad [8.1]$$

$$D^* = \frac{1}{2} \left(1 - \frac{\beta_0^2}{\alpha_0^2} \right) \times \left[\left(1 + \frac{4\delta^* \cos^2(\theta) \sin^2(\theta)}{(1 - \beta_0^2/\alpha_0^2)^2} + \frac{4(1 - \beta_0^2/\alpha_0^2 + \varepsilon)\varepsilon}{(1 - \beta_0^2/\alpha_0^2)^2} \cos^4(\theta) \right)^{1/2} - 1 \right] \quad [8.2]$$

$$\alpha_0 = \sqrt{\frac{C_{33}}{\rho}} \quad [8.3]$$

$$\beta_0 = \sqrt{\frac{C_{44}}{\rho}} \quad [8.4]$$

$$\varepsilon = \frac{C_{11} - C_{33}}{2C_{33}} \quad [8.5]$$

$$\delta^* = \frac{1}{2C_{33}^2} \Big(2(C_{13} + C_{44})^2 - (C_{33} - C_{44})(C_{11} + C_{33} - 2C_{44}) \Big) \quad [8.6]$$

α_0 and β_0 are the phase velocity of a compression wave and a shear wave with vertical polarization, respectively, in the direction of the symmetry axis. ε and δ^* are two parameters of anisotropy. These four parameters are determined by the elastic stiffnesses C_{ij} and the mass density ρ. θ is the phase angle between the wave vector and the plane of isotropy (i.e. a plane perpendicular to the axis of symmetry, see Figure 8.6).

During ultrasound image reconstruction, one needs the group velocity V (or ray velocity) and group angle ϕ (or ray angle). These can be calculated as follows (Thomsen 1986):

$$\tan\Big(\phi(\theta)\Big) = \left(\tan\theta + \frac{1}{v}\frac{\partial v}{\partial \theta} \right) \Big/ \left(1 - \frac{\tan\theta}{v}\frac{\partial v}{\partial \theta} \right) \quad [8.7]$$

$$V^2\Big(\phi(\theta)\Big) = v^2(\theta) + \left(\frac{\partial v}{\partial \theta} \right)^2 \quad [8.8]$$

v is the phase velocity of a shear or a compression wave (Equation 8.1), θ is the corresponding phase angle.

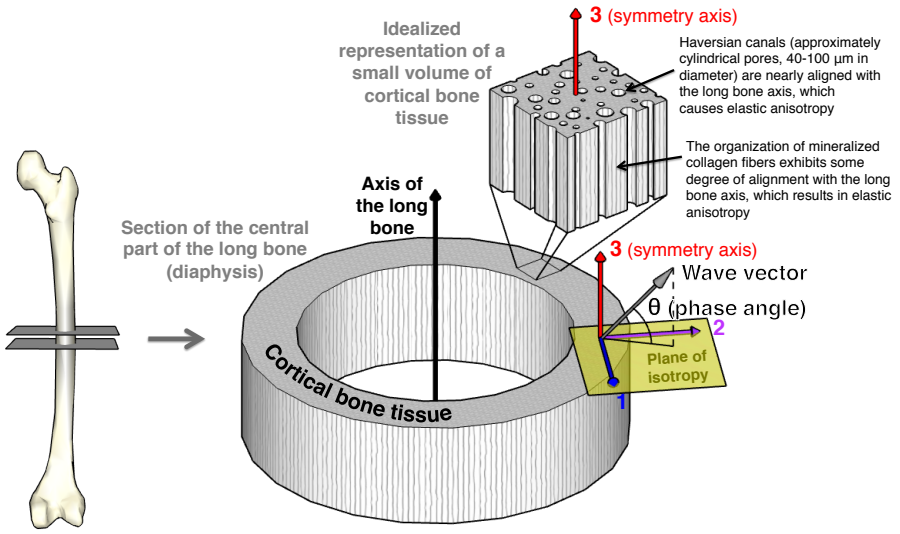

Figure 8.6 – Simplified representation of a section of the central part (diaphysis) of a long bone (for instance humerus, radius, femur, tibia bones). The local symmetry axis of the cortical bone tissue (coordinate axis 3) is nearly aligned with the long bone axis. The plane (1,2) (or any plane perpendicular to the symmetry axis) is a plane of wave speed isotropy. θ is the phase angle between the wave vector and the plane of isotropy.

Equation 8.1 can be used for image reconstruction, but a weak-anisotropy simplification proposed by seismologists (Thomsen 1986) is advantageous because it reduces computational time. If $|\delta^*| \ll 1$ and $|\varepsilon| \ll 1$, after full linearization of equations 8.1 and 8.2, the group velocity of a compression wave V_P can be approximated as:

$$V_P(\phi) = V_P^{axial} - (V_P^{axial} - V_P^{radial}) \times \left[\xi \sin^2(\phi)\cos^2(\phi) + \cos^4(\phi)\right] \quad [8.9]$$

ϕ is the group angle. $V_P^{radial} = \sqrt{C_{11}/\rho}$ is the compression wave speed in the plane of isotropy of cortical bone. $V_P^{axial} = \alpha_0 = \sqrt{C_{33}/\rho}$ is the compression wave speed in the direction of the symmetry axis of cortical bone. It is worth noting that $V_P^{radial} = V_P(\phi = 0) = v_P(\theta = 0)$ and $V_P^{axial} = V_P(\phi = \pi/2) = v_P(\theta = \pi/2)$. ξ is an anisotropy form parameter. Even though the conditions $|\delta^*| \ll 1$ and $|\varepsilon| \ll 1$ are not properly fulfilled in bone, it was shown that equation 8.9 allows ultrasound image reconstruction of the bone cortex with satisfying accuracy (Renaud *et al*. 2018), and it is computationally efficient for real-time imaging.
Figure 8.7 illustrates the wave speed anisotropy of a compressional wave (or P-wave) in cortical bone.

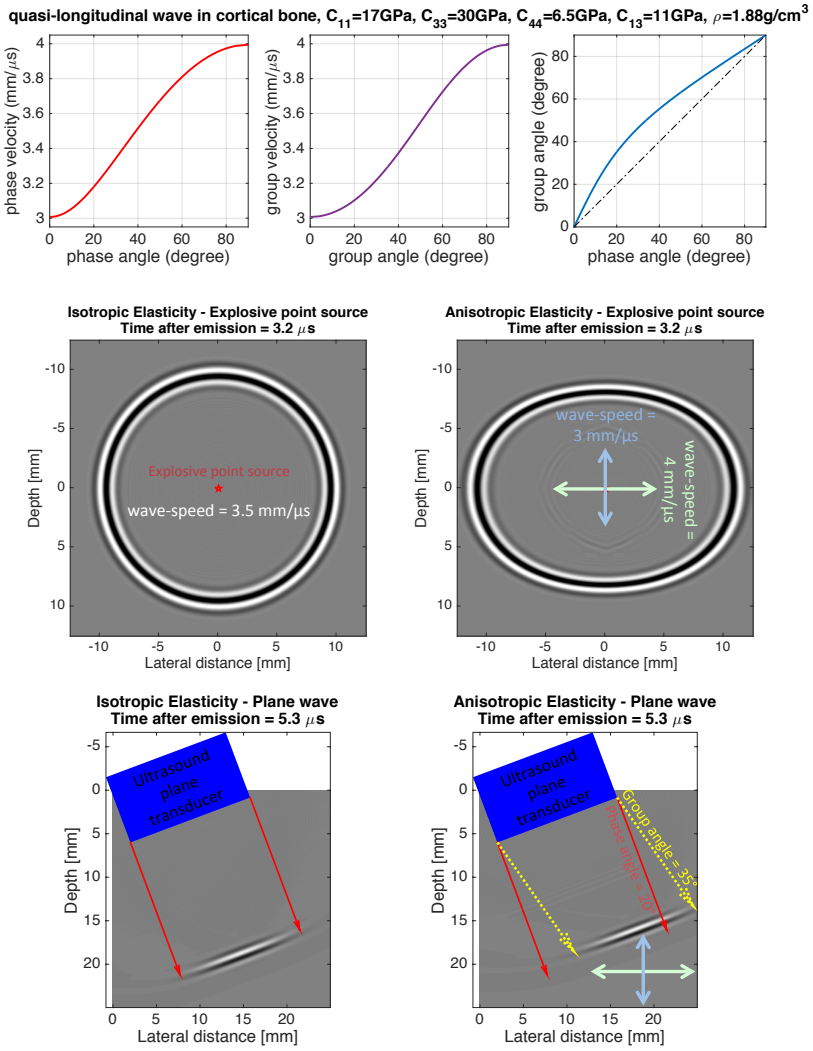

Figure 8.7 – Illustration of wave speed anisotropy for a compressional wave in human cortical bone. Top panels: phase and group velocities as functions of phase and group angles (phase angle $\theta = 90^o$ or group angle $\phi = 90^o$ corresponds to the direction of the symmetry axis). Middle panels: propagation of a wavefront generated by an explosive point source in a medium with isotropic and anisotropic elasticity. Bottom panels: propagation of a plane wavefront generated by a plane ultrasound transducer in a medium with isotropic and anisotropic elasticity.

Typical properties for human cortical bone (Bernard *et al*. 2016) were used to compute the wave speed anisotropy. It is seen that the compressional wave speed reaches a maximum value close to 4 mm/μs in the direction of the symmetry axis (*i.e.* approximately oriented along the main axis of a long bone for cortical bone tissue at the central part of the long bone). In a direction normal to the symmetry axis (*i.e.* a direction approximately perpendicular to the outer surface of a long bone at its midsection), the compressional wave speed exhibits a minimum value close to 3 mm/μs. For an oblique direction, unlike in a medium with isotropic elasticity, a plane wavefront generated by a planar transducer does not propagate in a direction normal to the surface of the transducer.

8.2.6. *Attenuation heterogeneity (shadowing and enhancement)*

Traditional B-mode imaging assumes that the backscattered echo amplitude (and thus brightness in the image) is determined by the target reflectivity. However, the backscattered echo amplitude is also influenced by the intrinsic attenuation of the tissues. During image reconstruction, the amplitude of echo signals is corrected assuming a uniform intrinsic attenuation, using an average value for biological soft tissue (0.5-1 dB/cm/MHz). If the ultrasound wave propagates through an inclusion with different intrinsic attenuation, the image brightness of the tissue surrounding this inclusion will not be constant. More specifically the region deeper than the inclusion but right behind it will appear with a different brightness while it should not since the inclusion is surrounded with the same tissue type. This situation is often encountered due to the presence of a fluid-filled cyst which exhibits much lower intrinsic attenuation compared to soft tissues. As a result, the region right behind the cyst shows enhanced brightness and can be misleading.
Conversely, a small region of calcified tissue (atherosclerotic plaque calcification, tendon calcification or bone) causes large reflection and attenuation loss. As a result, the deeper region just beyond the calcification shows highly reduced brightness. Although image reading is not possible in this strongly shadowed area, this artifact is useful to detect a calcification. An example using simulations is shown in Fig. 8.8. An anechoic lesion containing a lossless fluid is present in homogeneously attenuating tissue (1 dB/cm/MHz), as shown in image A. In image B, the calcification-like structure creates a shadow making structures right behind the calcification indiscernible.

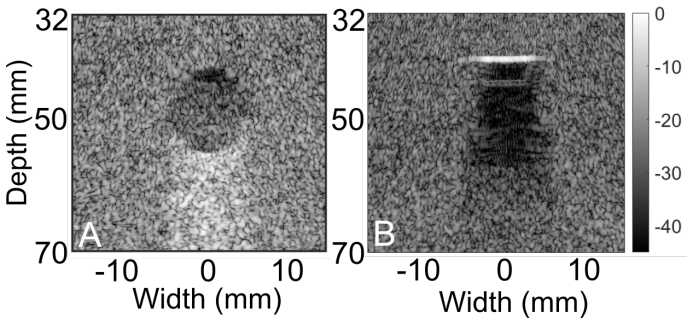

Figure 8.8 – B-mode image generated from a 5.5 MHz plane wave emission of (A) a 10 mm diameter anechoic, lossless lesion in a homogeneously attenuating medium (1 dB/cm/MHz) and (B) a calcification-like structure with an attenuation value of 10 dB/cm/MHz. Gray scale unit is in normalized dB.

8.3. Correction methods

8.3.1. *Need for correction techniques in diagnostic ultrasound*

The problem of phase aberration was extensively studied with the development of therapeutic applications of ultrasound, in particular for transcranial high-intensity focused ultrasound. Several solutions have been proposed to efficiently correct phase aberrations caused by the skull, for instance the use of a 3D scan of the skull made with x-ray computed tomography or magnetic resonance imaging to estimate, and subsequently correct for, phase aberrations.
Transcranial diagnostic ultrasound is, in fact, more challenging than transcranial therapeutic high-intensity focused ultrasound, for the following reasons:

– While a low ultrasound frequency (1 MHz) is considered optimal for transcranial therapeutic ultrasound, a higher ultrasound frequency ($\geq$ 3 MHz) is desired for transcranial diagnostic ultrasound in order to achieve satisfying spatial resolution.

– In transcranial therapeutic ultrasound, only forward propagation is considered and hence ultrasound traverses the skull once. In contrast, for transcranial diagnostic ultrasound, ultrasound waves experience phase aberrations twice, during both forward and backward propagation.

– Transcranial therapeutic ultrasound typically employs a highly focused beam. As a result, reverberation has low impact. In contrast, transcranial diagnostic ultrasound uses weakly focused beams and relies on the processing of small-amplitude echo signals. In this situation, reverberation caused by the skull becomes an important problem.

Diagnostic transcranial ultrasound imaging is routinely performed in hospitals. Unfortunately, image quality achieved with current clinical ultrasound scanners is

poor because the effect of the skull is ignored during image reconstruction. Several solutions have been investigated in the past four decades, but none of them has reached implementation in a clinical ultrasound scanner so far, for diagnostic transcranial ultrasound imaging. With the advent of ultrafast ultrasound imaging which relies on the use of unfocused transmit beams and synthetic focusing, new achievements have recently been made for cerebral blood flow measurements (Demené *et al*. 2021). In addition, ultrasound imaging of the cortex of long bones (Renaud *et al*. 2018) and ultrasound quantification of intraosseous blood flow (Salles *et al*. 2021) was recently demonstrated.

Several manufacturers of clinical ultrasound systems offer some degree of correction of the effect of the lower sound speed in fat in abdominal and breast exams. Many machine vendors also offer a technique that reduces multiple scattering occurring near the transducer, called tissue harmonic imaging (see section 8.15). Unfortunately, despite these dedicated developments, a significant number of patients remain difficult to scan (Philips-Healthcare 2008).

8.3.2. *Correction of phase aberration*

8.3.2.1. *Uniform sound speed correction*

Several modern ultrasound scanners offer automatic determination of the sound speed in the region of interest (Napolitano *et al*. 2006 ; Treeby *et al*. 2011 ; Gyöngy and Kollár 2015). This provides optimal image reconstruction if the scanned region is nearly homogeneous (*i.e.* weak aberration). One approach consists in reconstructing the image for different values of sound speed. The estimate of the sound speed is the value that provides the image with the largest sharpness. There exist multiple metrics of sharpness, for instance the normalized variance of the pixel intensity in the image or metrics based on spatial gradients (Treeby *et al*. 2011).
The synthetic data set for a uniform medium obtained with a numerical wave propagation solver shown in Figure 8.1 (panels a and c) is used to illustrate the use of a metrics of image sharpness to estimate the sound speed. The true sound speed in this numerical model is 1540 m/s. Figure 8.9 shows that if the sound speed is larger or smaller than this value, the two metrics of image sharpness decreases.

When using the synthetic data set for the abdominal wall model (panels b and d in Figure 8.1), the two metrics of image sharpness show multiple peaks as shown in Figure 8.10. The optimal image sharpness is found for a sound speed of 1490 m/s. However the image quality obtained with a sound speed of 1490 m/s (panel c in Figure 8.10) is not significantly improved, compared to the image reconstructed with a default sound speed of 1540 m/s. Therefore the approach fails in medium with rather strong aberration. More advanced techniques are required to improve image quality, like those described in the following sections.

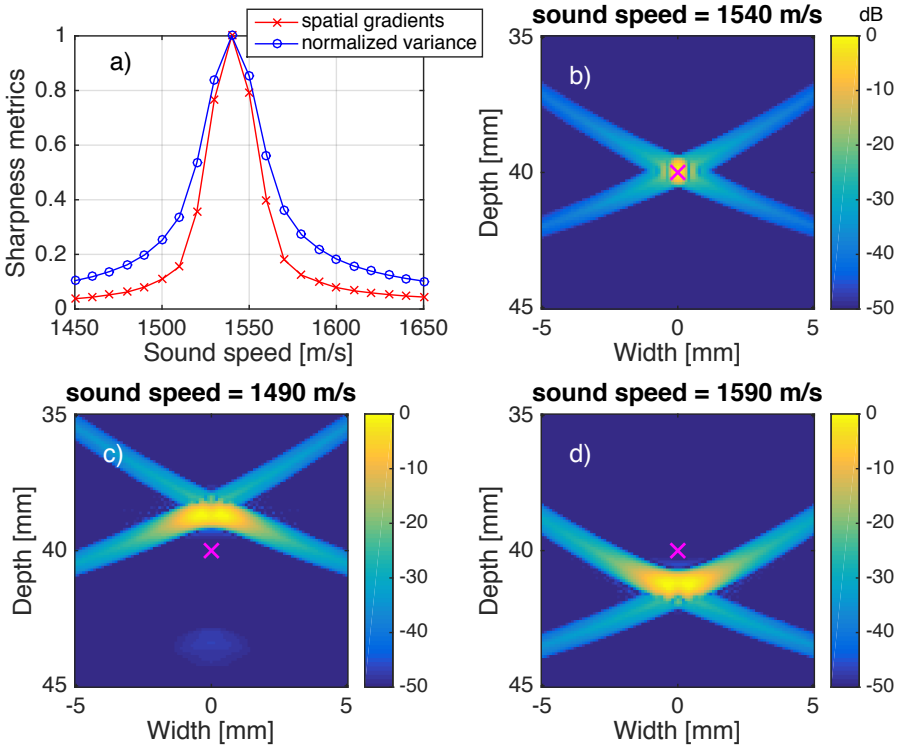

Figure 8.9 – Illustration of a method for estimating the sound speed in a homogeneous medium (same data as in Figure 8.1). Panel a) shows the sharpness metrics (normalized variance of the pixel intensity and spatial gradients in the image) as a function of the sound speed. It peaks for a sound speed of 1540 m/s, which is the true sound speed in this numerical model. Panels b), c) and d) show the reconstructed image for three different values of sound speed. The cross indicates the true position of the point source.

8.3.2.2. *"Blind" methods, not trying to describe the medium geometry or estimate a sound speed map*

The only approaches for aberration correction that reached real-time implementation on an ultrasound scanner use a near-field phase screen model (Trahey *et al*. 1990 ; Liu *et al*. 2000 ; Rigby *et al*. 2000 ; Dahl *et al*. 2006). This model is simple, it assumes that the distortion of the received wavefront is predominantly caused by a thin aberrating layer very near the transducer surface. This approach was very recently released on a clinical system, without any reduction of imaging rate (Masoy *et al*. 2022).
Early studies proposed to estimate arrival time fluctuations in the receiving aperture (after geometric correction of the arrival time) by means of two techniques:

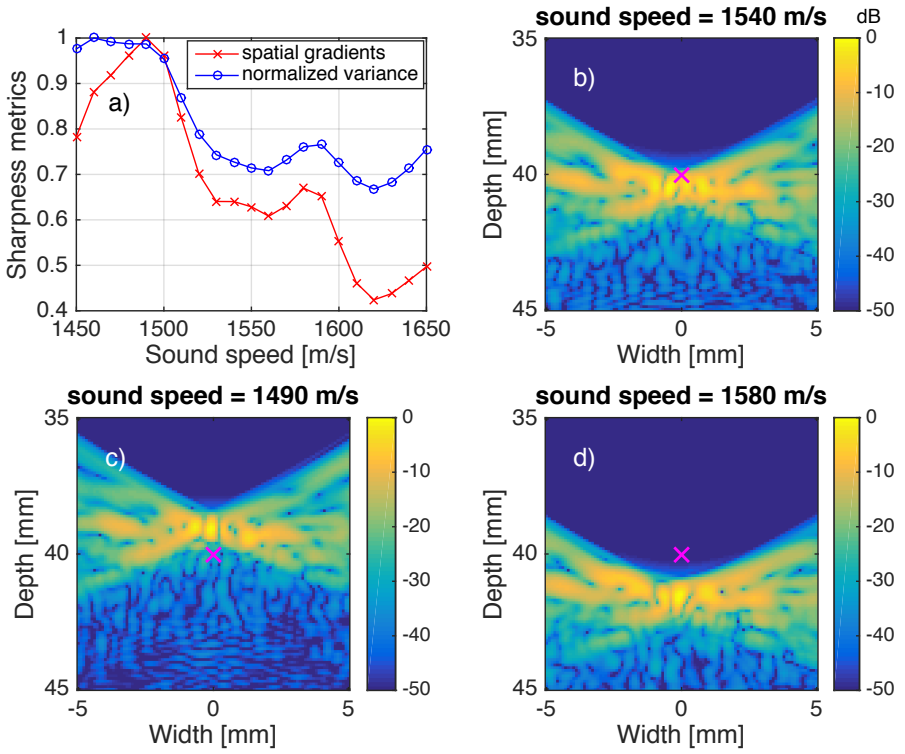

Figure 8.10 – Illustration of a method for estimating the average sound speed with the abdominal wall model (same data as in Figure 8.1). Panel a) shows the sharpness metrics (normalized variance of the pixel intensity and spatial gradients in the image) as a function of the sound speed. Multiple peaks are found. Panels b), c) and d) show the reconstructed image for three different values of sound speed. The cross indicates the true position of the point source.

– cross-correlations between raw echo signals recorded by individual elements of the transducer array (O'donnell and Flax 1988*a*),

– iterative adjustment of the transmit and receive phasing of individual or groups of elements in order to reach maximum brightness of the speckle in a region of interest (Nock *et al*. 1989).

The two approaches and another one that used a waveform similarity factor as a quality factor (instead of the regional speckle brightness) (Liu *et al*. 2000) are in fact equivalent since they all try to realign the arrival times of the echo signals in the receive aperture (Ng *et al*. 1994).
It is interesting to note that the techniques can be applied to the wavefront arising from

a small bright target (for instance a small calcification) or from the focal region in tissue (with sub-wavelength heterogeneities) with transmit beam focusing (van Cittert-Zernicke theorem (Mallart and Fink 1994)).
The synthetic data sets obtained with a numerical wave propagation solver shown in Figure 8.1 are now used to illustrate the cross-correlation technique as described in (Rigby *et al*. 2000). The method correlates individual element signals with a common reference signal, called the beamsum, obtained by summing all echo signals in the receive aperture (after geometric correction of the arrival time). Once the arrival time fluctuations are estimated, element-based time shifting of the echoes improves focusing as shown in Figure 8.11. Traditional ultrasound imaging relies on the transmission of focused beams. Phase aberration correction improves focusing both in transmit and receive. Because phase aberration correction improves the shape of the transmit focused beam, the technique can be implemented iteratively in order to improve the estimation of the arrival time fluctuations (Rigby *et al*. 2000). A limitation of this technique is that the resulting image may be linearly translated to some unknown amount from its correct position, as shown in panel d) of Figure 8.11 (Rachlin 1990).

The acoustic inhomogeneities (mass density and wavespeed) are often not only located near the array transducer, they are distributed in the region of interest. As a result the received wavefront is not only distorted by local time-shifting, its amplitude and shape are also distorted through diffraction, refraction and multiple scattering. Applying a near-field phase screen model to a medium with distributed aberration provides optimal phase aberration correction only in a limited region, called the isoplanatic patch. Because the size of the isoplanatic patch is often smaller than the size of the scanned volume, phase aberration correction must be applied to multiple sub-regions of the scanned volume (Lindsey and Smith 2013). Generally, the stronger the aberration the smaller the size of the isoplanatic patch.
An improvement of the near-field phase screen model has been proposed by Liu and Waag (Liu and Waag 1994). It consists in moving the phase screen in depth by back-propagating the echo signals recorded by the transducer array. The optimal depth of the phase screen is obtained by maximizing a waveform similarity factor.
Perhaps the most advanced technique is based on time reversal acoustics (Montaldo *et al*. 2011). An iterative procedure relying on the broadcasting of the time-reversed version of echo signals recorded by individual transducer elements is capable of retrieving the Green's function between a point in the scanned volume and the transducer array in a heterogeneous medium. However the technique requires sophisticated equipment since the ultrasound scanner must be able to send back to the medium a time-reversed version of echo signals. This approach allows for correction of all sources of aberration (diffraction, refraction and multiple scattering), however optimal aberration correction is still restricted to a limited region (isoplanatic patch). Nonetheless very recent work has proposed a method to estimate pixel-based optimal focusing delays, therefore potentially reducing the size of the isoplanatic patch to a single image pixel (Lambert *et al*. 2020). It relies on the construction of distortion

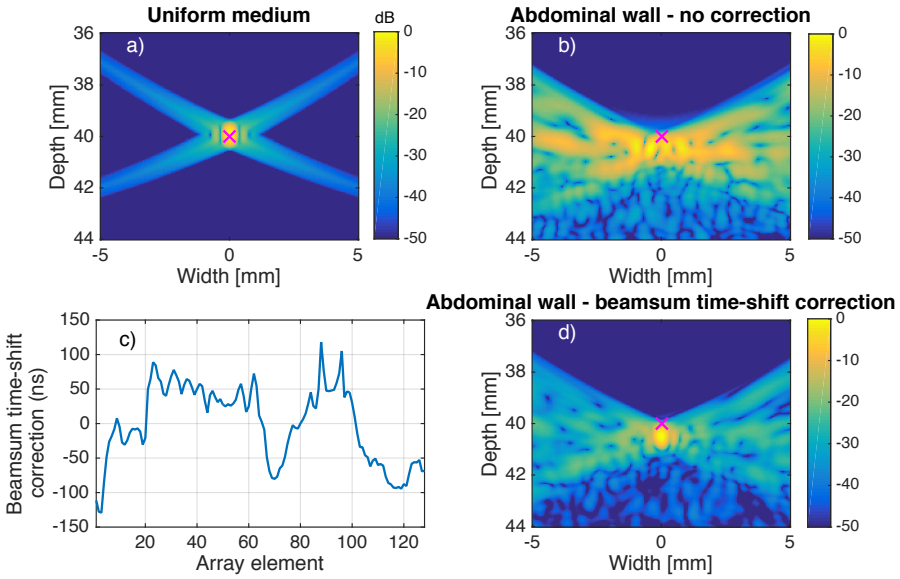

Figure 8.11 – Illustration of a phase aberration correction method called the cross-correlation method. Panels a) and b) show the reconstructed images of a point source, using the same synthetic data sets shown in Figure 8.1, in a perfectly homogeneous medium and behind an abdominal wall model. Panel c) shows the aberration profile obtained with a cross-correlation method called beamsum (Rigby *et al.* 2000). Panel d) shows the improvement of the reconstructed image of the point source behind the abdominal wall model, if element-based time shifting of the echoes is applied using the aberration profile shown in panel c). The cross indicates the true position of the point source.

matrix and its time-reversal analysis, which enables the estimation of a transmission matrix between each array element and each image pixel.

Transcranial ultrasound imaging through the temporal bone of the skull is very challenging because the skull generates strong aberration. The near-field phase screen approach was investigated for transcranial ultrasound imaging with limited success (Ivancevich *et al*. 2008). Another approach using two transducers placed over opposing temporal acoustic windows was proposed (Phillips *et al*. 1975*a* ; Vignon *et al*. 2006 ; Lindsey and Smith 2013), in this way the aberration profile can be learned near the receiving transducer with one-way through transmission between the two transducers. Nonetheless the phase aberration correction remained optimal in a sub-region of the image therefore the phase aberration correction had to be performed in multiple sub-regions of the scanned volume (multiple isoplanatic patches) (Lindsey and Smith 2013).

8.3.2.3. *Descriptive methods trying to determine the medium geometry and estimate a sound speed map*

Instead of assuming that aberration is predominantly caused by a thin layer very near the transducer, it was proposed to describe aberration as caused a layer with a finite thickness in contact with the transducer (Smith *et al*. 1986 ; Lindsey and Smith 2014). The scanned volume is then described with two homogeneous layers with different sound speeds. The advantage compared to the near-field phase screen model is that refraction through the aberrating layer is taken into account. In fact, this approach aimed to solve the problem of isoplanatic patch of near-field phase screen techniques (see Section 8.3.2.2). However these first attempts had limited success, likely because the thickness of the aberrating layer was assumed constant and its value is predetermined by the operator. The sound speed in the aberrating layer was also predetermined by the operator. In addition, the aberrating layer was considered parallel to the surface of the transducer and in contact with the transducer.
Recently, this approach was extended to an aberrating layer whose thickness was not assumed constant and parallel to the transducer. The near and far surfaces of aberrating layer were searched during the image reconstruction. Each layer was assumed homogeneous, the sound speed was estimated in each layer with a technique similar to the approach described in Section 8.3.2.1. As a result, refraction is more accurately modeled. The approach was applied to intraosseous ultrasound imaging for imaging the central part of a long bone (Renaud *et al*. 2018) and transcranial ultrasound imaging through the temporal window (Mozaffarzadeh, Verschuur, Verweij, Daeichin, de Jong and Renaud 2022 ; Mozaffarzadeh, Verschuur, Verweij, de Jong and Renaud 2022*a*,*b*). Figure 8.12 shows an example of *in vivo* images of the cortex of the central part of a human tibia.
Finally, a last family of techniques (Jaeger *et al*. 2015 ; Sanabria *et al*. 2018) attempts to recover a sound speed map of the scanned region similarly to ultrasound tomography (Wiskin *et al*. 2019), which required a dedicated equipment capable of transmitting and receiving ultrasound waves all around the scanned object, but with single-sided pulse-echo ultrasound imaging.

8.3.3. *Correction of anisotropic elasticity in bone*

The anisotropic elasticity of cortical bone makes ultrasound image reconstruction in a region including bone more challenging than for a region consisting of heterogeneous soft tissues only. The transmission of a plane wave, scattering by a small point target at 14 mm depth, and recording with a 2.5 MHz phased-array transducer was simulated numerically with the software SimSonic (Bossy *et al*. 2002). The wave speed anisotropy in cortical bone was modeled with the parameters used to plot Figure 8.7. Figure 8.13 compares the point spread function in a) an ideal uniform medium with a wave speed of 1.5 mm/μs, b) in cortical bone with wave speed anisotropy modeled during image reconstruction and c) in cortical bone with wave speed anisotropy

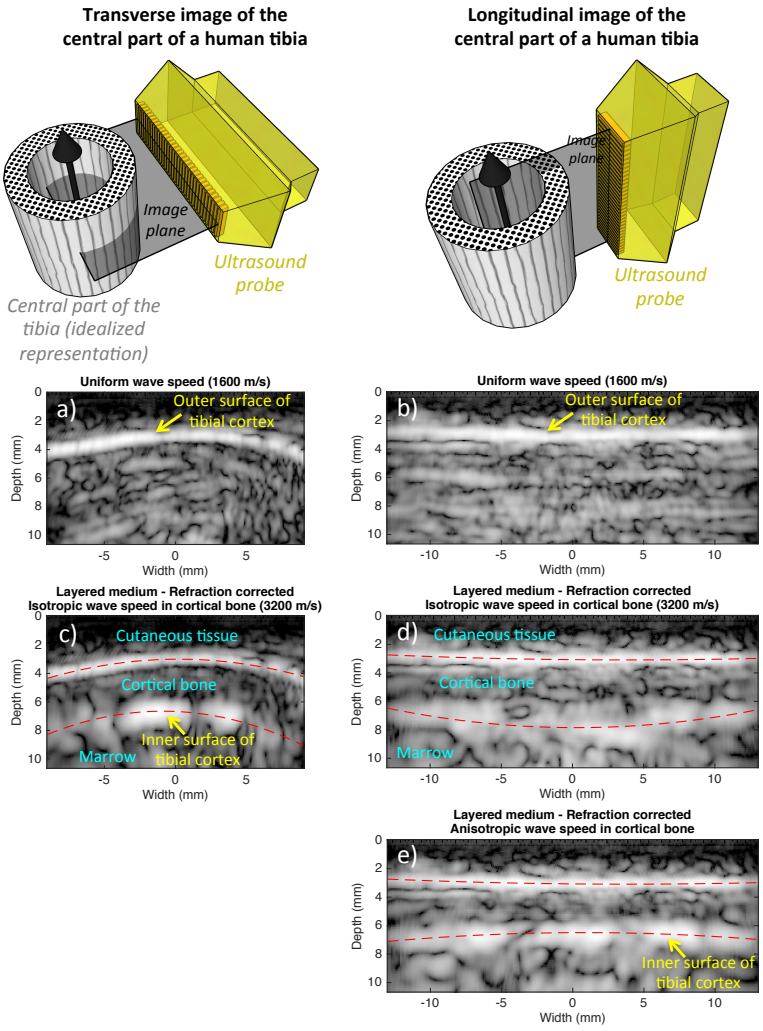

Figure 8.12 – *In vivo* images of the cortex of the central part of a human tibia obtained with synthetic aperture imaging. A phased array transducer with 96 elements was used, the center frequency of the transmit short burst was 2.5 MHz. Panels a) and b) show transverse and longitudinal images as obtained with traditional image reconstruction (uniform wave speed). Panels c) and d) show transverse and longitudinal images as obtained if the medium is described with two layers (cutaneous tissue and cortical bone), the wave speed in cortical bone is isotropic. Panel e) demonstrates that the correction of wave speed anisotropy improves the image of the bone cortex. Displayed dynamic range is 40 dB.

ignored during image reconstruction. A significant degradation of the point spread function occurs in cortical bone if wave speed anisotropy is ignored. Figure 8.14 similarly shows the degradation of the point spread function in a region of soft tissue separated from the transducer by a layer of cortical bone (5 mm thick). The images in Figures 8.13 (b) and 8.14 (b) are reconstructed with the approach described in (Renaud *et al*. 2018, 2020), which can take into account refraction and wave speed anisotropy in a layered medium.

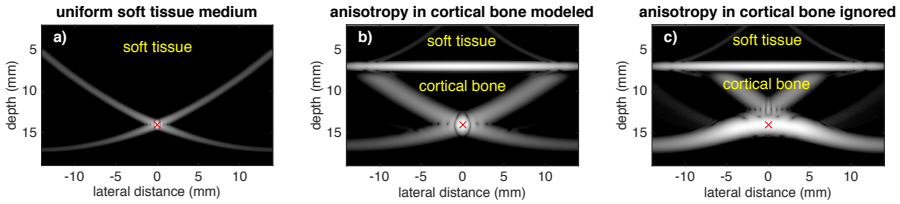

Figure 8.13 – Illustration of the importance of wave speed anisotropy in cortical bone with *in silico* data. Point spread function obtained from a point target at a 14-mm depth (shown by a red cross) a) in a uniform medium with isotropic wave speed (1.5 mm/μs), b) in cortical bone with wave speed anisotropy modeled during image reconstruction (using the characteristics shown in Figure 8.7), c) in cortical bone with wave speed anisotropy ignored during image reconstruction (an isotropic wave speed of 3 mm/μs is used). Displayed dynamic range is 60 dB.

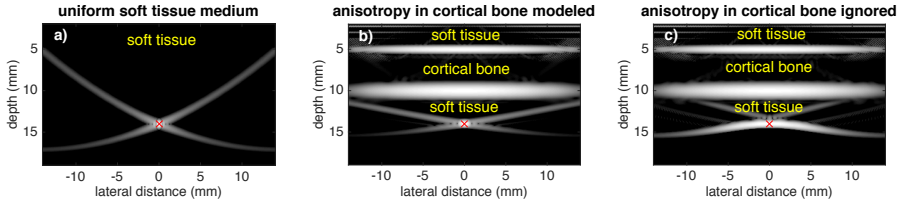

Figure 8.14 – Illustration with *in silico* data of the importance of wave speed anisotropy when imaging a layer of soft tissue separated from the transducer by a layer of cortical bone. Point spread function obtained from a point target at 14 mm depth (shown by a red cross) a) in a uniform medium with isotropic wave speed (1.5 mm/μs), b) in soft tissue under a layer of cortical bone with wave speed anisotropy in the bone layer modeled during image reconstruction (using the characteristics shown in Figure 8.7), c) in soft tissue under a layer of cortical bone with wave speed anisotropy in the bone layer ignored during image reconstruction (an isotropic wave speed of 3 mm/μs is used). Displayed dynamic range is 60 dB.

With these idealized two-dimensional *in silico* datasets, ignoring wave speed anisotropy in cortical bone does not seem to degrade the image of the far surface of

the cortical bone layer (see 10 mm depth in panel c) of Figure 8.14). However, panel e) in Figure 8.12 shows that the correction of wave speed anisotropy significantly improves the detection of the inner surface of the tibial cortex with *in vivo* data. Equation 8.9 was used with $V_P^{axial} = 4$ mm/μs, V_P^{radial}= 3.2 mm/μs and $\xi = 1.6$.

8.3.4. *Reduction of multiple scattering with tissue harmonic imaging*

Tissue harmonic imaging demonstrated improved image quality in transcranial ultrasound imaging (Puls *et al*. 2000) and ultrasound echocardiography (Spencer *et al*. 1998). In addition to improving the spatial lateral resolution in the ultrasound image and reducing clutter signal caused by the side lobes and grating lobes of the transmit beam, tissue harmonic imaging reduces clutter signal caused by reverberation occurring in heterogeneous tissue layers close to the transducer.
Tissue harmonic imaging relies on nonlinear ultrasound propagation. Nonlinear propagation distorts the waveform output by the transducer. This distortion progressively builds up as the wave propagates. If analyzed in the frequency domain, this progressive distortion corresponds to the generation of new frequency components that were absent in the waveform generated by the transducer. The largest new component is created at twice the ultrasound frequency generated by the transducer, which is often called the second harmonic component (sometimes also called first harmonic). For a transmit focused or unfocused beam, there exist two phases. During the first phase, between the transducer and a certain distance, the amplitude of the second harmonic component increases from zero to a maximum value. During the second phase, for larger distances, the amplitude of the second harmonic component decays progressively because the effect of attenuation overwhelms the effect of nonlinear propagation. In first approximation, the amplitude of the second harmonic component is proportional to the squared amplitude at the transmit frequency. It is worth noticing that linear backward propagation of echoes can be assumed because they have small amplitude. Therefore tissue harmonic imaging reduces reverberation clutter in transmit only (forward propagation), not during backward propagation of echoes.
Tissue harmonic imaging is now implemented in most clinical ultrasound scanners. The use of dedicated pulse sequences, like pulse inversion or amplitude modulation, enables the extraction of the second harmonic component.

Harmonic imaging can circumvent reverberation clutter as a mechanism for image degradation because of its low amplitude in the near field where most of the reverberations occur. Trailing clutter can also potentially be reduced, given it is generated in the near field, because of its low amplitude which makes it less prone to nonlinear distortion compared to the main pulse. Most of the energy in the pulse tail will remain in the fundamental frequency with propagation and will not appear in the harmonic image (Pinton, Dahl and Trahey 2009)).

Figure 8.15 illustrates the reduction of near-field reverberation clutter achieved with tissue harmonic imaging. Using a numerical wave solver (k-wave (Treeby *et al.* 2012)), nonlinear propagation of a plane wave was computed through heterogeneous tissue layers located near the transducer. It is seen that the relative magnitude of the trailing signal caused by reverberation in the second harmonic component is smaller than that in the full signal. As a result, reconstructing an ultrasound image with the second harmonic component produces an image with reduced reverberation clutter. The improvement is larger with transmit focused beams because the second harmonic component starts to build up at a distance deeper than the tissue layers (near the probe) that are responsible for reverberations (this distance is determined by the transmit focus depth and depth-of-field).

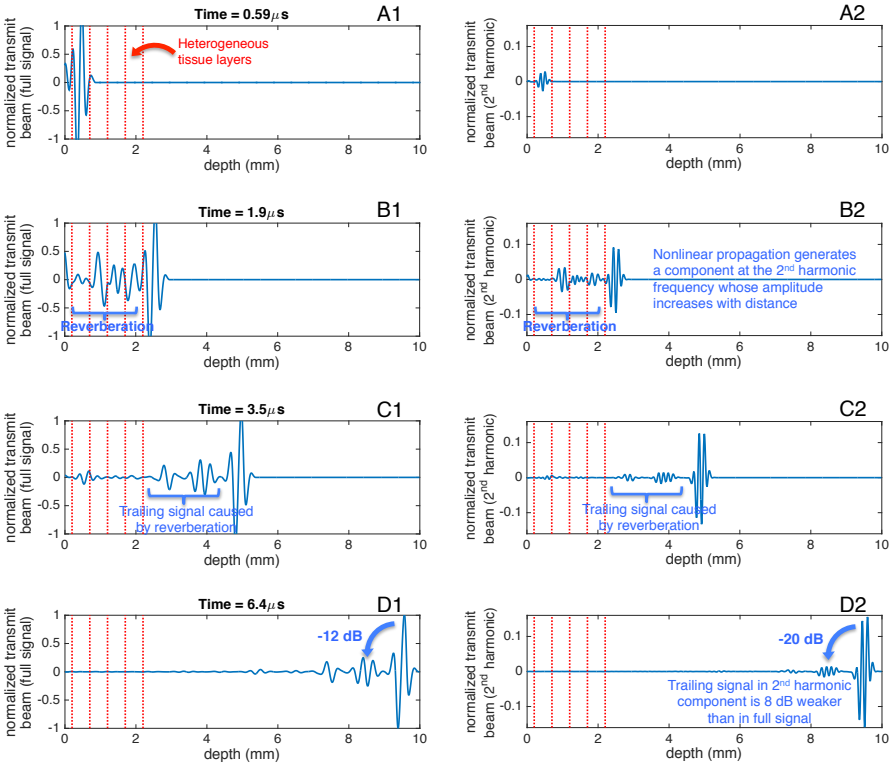

Figure 8.15 – Illustration of tissue harmonic imaging with a numerical simulation in a one-dimensional space. A 5-MHz short pulse is generated by a source located at depth = 0. Four heterogeneous layers are placed near the source. Panels A1-B1-C1-D1 are snapshots at four different instants showing the full waveform. Panels A2-B2-C2-D2 are snapshots at the same four instants showing the second harmonic component (10 MHz) extracted from the full waveform with pulse inversion.

Figure 8.16 illustrates the improvement in the PSF/ambient clutter ratio in 2D in tanscranial imaging. A 1.25 Mhz single focus transmit at 50 mm is used to generate images of a point target in a homogeneous medium (panels B1 and B2) and transcranially (panels C1 and C2) through the sound speed map shown in panel A. In panel D, the midline in images C1 and C2 as a function of depth illustrates how harmonic imaging decreases the relative amplitude of the ambient clutter around the target by about 20 dB in the transcranial image.

Instead of reducing the importance of multiple scattering during the acquisition like tissue harmonic imaging, advanced signal post-processing was also proposed to remove multiple reflections from the recorded echo signals (Lambert *et al*. 2020).

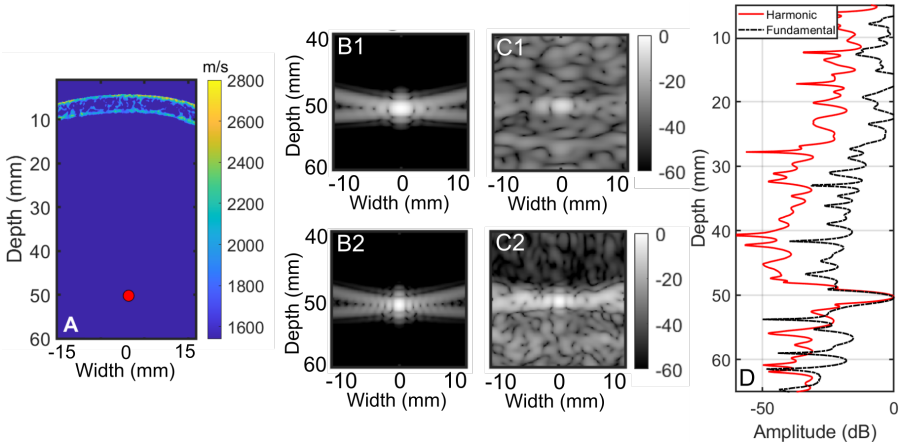

Figure 8.16 – Simulation derived B-mode images for a 1.25MHz emission in a homogeneous medium (B1,B2) and transcranially (C1,C2) for the fundamental at 1.25 Hz (B1,C1) and the second harmonic frequency at 2.5 MHz (B2,C2). A 2 cycle single focused transmit focusing at 50 mm is used. (A) shows the sound speed map of the human skull slice used to generate images (C1) and (C2). Target size is exaggerated. In (D) the midline of C1 and C2 as a function of depth is plotted.

8.4. Current limitations for correcting the sources of image degradation and future

8.4.1. *Need for matrix array and high computational power*

Most clinical transducers for 2D ultrasound imaging are still one-dimensional arrays, where the height of the elements (in the elevation dimension, *i.e.* the dimension normal to the image plane) is typically between 5 and 15 mm. These transducers are unable to correct for phase aberration in the elevation dimension because they do

not spatially sample the recorded echo wavefronts in this dimension. Therefore, early work on aberration correction has advertised the need for two-dimensional arrays. Research has suggested that an elevation pitch at least 75%, but perhaps as fine as 25 to 30% of the aberration correlation length, might be needed for effective aberration measurements and therefore the correction of phase aberration (Lacefield and Waag 2001). Two-dimensional arrays are becoming more and more available. An additional requirement for phase aberration correction is access to raw echo signals on each individual elements of the array. This often represents a large amount of data, which needs to be processed with high-performance computers.

8.4.2. *Real-time versus offline aberration correction*

Until recently, real-time implementations of phase aberration correction on ultrasound scanner have achieved rather low imaging rates between 0.5 and 8.5 frames per second (Dahl *et al*. 2006), because phase aberration correction requires advanced strategies and signal processing. In 2022, GE Heathcare released a phase aberration correction, based on a near-field phase screen approach, operating in real-time at $\sim$100 frames per second with a matrix array transducer (Masoy *et al*. 2022). When image degradation is strong, with two-dimensional arrays becoming more and more available, hand-held 2D ultrasound imaging may shift towards 4D (3D+time) ultrasound imaging with the transducer being held static in front of the region of interest with dedicated equipment. In these very challenging situations, the future ultrasound scanner may first acquire volumetric ultrasound data for a few seconds, likely including iterative strategies to characterize and mitigate the sources of image degradation during the acquisition, and reconstruct high-quality images in a second step, after post-processing of the acquired data.

8.4.3. *Blood flow quantification*

Ultrasound characterization of blood flow is commonly achieved by analyzing the non-stationary components of the ultrasound image, which correspond to moving red blood cells. Ultrasound contrast agents made of gas microbubbles are also used as a surrogate for the blood signal. Both red blood cells and microbubbles are much smaller than the ultrasound wavelength, therefore they can be seen as point targets. Thus the image of a single red blood cell or microbubble is a point spread function. Just like image quality, blood flow quantification is corrupted if the point spread function is degraded by aberration or multiple scattering. In particular, a degraded PSF results in degraded spatial specificity of the information on blood flow. Consequently, the correction of aberration and the reduction of multiple scattering are crucial because they improve both image quality and blood flow quantification.

8.5. Bibliography

Alexander, S. L., Rafaels, K., Gunnarsson, C. A., Weerasooriya, T. (2019), Structural analysis of the frontal and parietal bones of the human skull, *Journal of the Mechanical Behavior of Biomedical Materials*, 90, 689–701.

Ashman, R., Cowin, S., Van Buskirk, W., Rice, J. (1984), A continuous wave technique for the measurement of the elastic properties of cortical bone, *Journal of Biomechanics*, 17(5), 349–361.

Bernard, S., Schneider, J., Varga, P., Laugier, P., Raum, K., Grimal, Q. (2016), Elasticity–density and viscoelasticity–density relationships at the tibia mid-diaphysis assessed from resonant ultrasound spectroscopy measurements, *Biomechanics and Modeling in Mechanobiology*, 15(1), 97–109.

Bossy, E., Talmant, M., Laugier, P. (2002), Effect of bone cortical thickness on velocity measurements using ultrasonic axial transmission: A 2d simulation study, *The Journal of the Acoustical Society of America*, 112(1), 297–307.

Dahl, J. J., Mcaleavey, S. A., Pinton, G. F., Soo, M. S., Trahey, G. E. (2006), Adaptive imaging on a diagnostic ultrasound scanner at quasi real-time rates, *IEEE Transactions on Ultrasonics, Ferroelectrics, and Frequency Control*, 53(10), 1832–1843.

Demené, C., Robin, J., Dizeux, A., Heiles, B., Pernot, M., Tanter, M., Perren, F. (2021), Transcranial ultrafast ultrasound localization microscopy of brain vasculature in patients, *Nature Biomedical Engineering*, 5(3), 219–228.

Freiburger, P. D., Sullivan, D. C., LeBlanc, B. H., Smith, S. W., Trahey, G. E. (1992), Two dimensional ultrasonic beam distortion in the breast: In vivo measurements and effects, *Ultrasonic Imaging*, 14(4), 398–414.

Granke, M., Grimal, Q., Saied, A., Nauleau, P., Peyrin, F., Laugier, P. (2011), Change in porosity is the major determinant of the variation of cortical bone elasticity at the millimeter scale in aged women, *Bone*, 49(5), 1020–1026.

Gyöngy, M., Kollár, S. (2015), Variation of ultrasound image lateral spectrum with assumed speed of sound and true scatterer density, *Ultrasonics*, 56, 370–380.

Hinkelman, L. M., Liu, D.-L., Metlay, L. A., Waag, R. C. (1994), Measurements of ultrasonic pulse arrival time and energy level variations produced by propagation through abdominal wall, *The Journal of the Acoustical Society of America*, 95(1), 530–541.

Hinkelman, L. M., Liu, D., Waag, R. C., Zhu, Q., Steinberg, B. D. (1995), Measurement and correction of ultrasonic pulse distortion produced by the human breast, *The Journal of the Acoustical Society of America*, 97(3), 1958–1969.

Hoskins, P. R., Martin, K., Thrush, A. (2019), *Diagnostic Ultrasound: Physics and Equipment (3rd Edition)*, CRC Press.

Ivancevich, N. M., Pinton, G. F., Nicoletto, H. A., Bennett, E., Laskowitz, D. T., Smith, S. W. (2008), Real-time 3-d contrast-enhanced transcranial ultrasound and

aberration correction, *Ultrasound in Medicine Biology*, 34(9), 1387–1395.

Jaeger, M., Robinson, E., Akarcay, H. G., Frenz, M. (2015), Full correction for spatially distributed speed-of-sound in echo ultrasound based on measuring aberration delays via transmit beam steering, *Physics in Medicine & Biology*, 60(11), 4497–4515.

Lacefield, J., Waag, R. (2001), Time-shift estimation and focusing through distributed aberration using multirow arrays, *IEEE Transactions on Ultrasonics, Ferroelectrics, and Frequency Control*, 48(6), 1606–1624.

Lagravere, M., Fang, Y., Carey, J., Toogood, R., Packota, G., Major, P. (2006), Density conversion factor determined using a cone-beam computed tomography unit newtom qr-dvt 9000, *Dentomaxillofacial Radiology*, 35(6), 407–409.

Lambert, W., Cobus, L. A., Frappart, T., Fink, M., Aubry, A. (2020), Distortion matrix approach for ultrasound imaging of random scattering media, *Proceedings of the National Academy of Sciences*, 117(26), 14645–14656.

Lindsey, B. D., Smith, S. W. (2013), Pitch-catch phase aberration correction of multiple isoplanatic patches for 3-d transcranial ultrasound imaging, *IEEE Transactions on Ultrasonics, Ferroelectrics, and Frequency Control*, 60(3), 463–480.

Lindsey, B. D., Smith, S. W. (2014), Refraction correction in 3d transcranial ultrasound imaging, *Ultrasonic imaging*, 36(1), 35–54.

Liu, D.-L., Sutcliffe, P., McDermott, B., Lazenby, J., von Behren, P., Kim, J. (2000), Adaptive ultrasonic imaging using sonoline elegra/sup tm/, *2000 IEEE Ultrasonics Symposium. Proceedings*, 2, 1655–1658.

Liu, D.-L., Waag, R. (1995), A comparison of ultrasonic wavefront distortion and compensation in one-dimensional and two-dimensional apertures, *IEEE Transactions on Ultrasonics, Ferroelectrics, and Frequency Control*, 42(4), 726–733.

Liu, D., Waag, R. C. (1994), Correction of ultrasonic wavefront distortion using backpropagation and a reference waveform method for timeâshift compensation, *The Journal of the Acoustical Society of America*, 96(2), 649–660.

Mallart, R., Fink, M. (1994), Adaptive focusing in scattering media through soundâspeed inhomogeneities: The van cittert zernike approach and focusing criterion, *The Journal of the Acoustical Society of America*, 96(6), 3721–3732.

Marquet, F., Pernot, M., Aubry, J.-F., Montaldo, G., Marsac, L., Tanter, M., Fink, M. (2009), Non-invasive transcranial ultrasound therapy based on a 3d CT scan: protocol validation andin vitroresults, *Physics in Medicine and Biology*, 54(9), 2597–2613.

Marsac, L., Chauvet, D., Greca, R. L., Boch, A.-L., Chaumoitre, K., Tanter, M., Aubry, J.-F. (2017), Ex vivo optimisation of a heterogeneous speed of sound model of the human skull for non-invasive transcranial focused ultrasound at 1âmhz, *International Journal of Hyperthermia*, 33(6), 635–645.

Masoy, S.-E., Denarie, B., Sornes, A., Holte, E., Grenne, B., Espeland, T., Berg, E. A. R., Rindal, O. M. H., Rigby, W., Bjastad, T. (2022), Aberration correction in 2d echocardiography, *preprint*, pp. 1–10.

Montaldo, G., Tanter, M., Fink, M. (2011), Time reversal of speckle noise, *Phys. Rev. Lett.*, 106, 054301.

Mozaffarzadeh, M., Verschuur, E., Verweij, M. D., Daeichin, V., de Jong, N., Renaud, G. (2022), Refraction-corrected transcranial ultrasound imaging through the human temporal window using a single probe, *IEEE Transactions on Ultrasonics, Ferroelectrics, and Frequency Control*, 69(4), 1191–1203.

Mozaffarzadeh, M., Verschuur, E., Verweij, M. D., de Jong, N., Renaud, G. (2022*a*), Accelerated 2-d real-time refraction-corrected transcranial ultrasound imaging, *IEEE Transactions on Ultrasonics, Ferroelectrics, and Frequency Control*, 69(9), 2599–2610.

Mozaffarzadeh, M., Verschuur, E., Verweij, M. D., de Jong, N., Renaud, G. (2022*b*), Comparison of phase-screen and geometry-based phase aberration correction techniques for real-time transcranial ultrasound imaging, *Applied Sciences*, 12(19), 10183.

Napolitano, D., Chou, C., McLaughlin, G., Ji, T., Mo, L., DeBusschere, D., Steins, R. (2006), Sound speed correction in ultrasound imaging, *Ultrasonics*, 44, Supplement, e43 – e46.

Ng, G., Worrell, S., Freiburger, P., Trahey, G. (1994), A comparative evaluation of several algorithms for phase aberration correction, *IEEE Transactions on Ultrasonics, Ferroelectrics, and Frequency Control*, 41(5), 631–643.

Nock, L., Trahey, G. E., Smith, S. W. (1989), Phase aberration correction in medical ultrasound using speckle brightness as a quality factor, *The Journal of the Acoustical Society of America*, 85(5), 1819–1833.

O'donnell, M., Flax, S. (1988*a*), Phase-aberration correction using signals from point reflectors and diffuse scatterers: Measurements, *IEEE transactions on ultrasonics, ferroelectrics, and frequency control*, 35(6), 768–774.

O'Donnell, M., Flax, S. (1988*b*), Phase aberration measurements in medical ultrasound: Human studies, *Ultrasonic imaging*, 10(1), 1–11.

Peterson, J., Dechow, P. C. (2003), Material properties of the human cranial vault and zygoma, *The Anatomical Record Part A: Discoveries in Molecular, Cellular, and Evolutionary Biology*, 274A(1), 785–797.

Philips-Healthcare (2008), Results of a technically difficult patient study - six sites in north america and europe, *White paper*, pp. 1–8.

Phillips, D., Smith, S., von Ramm, O., Thurstone, F. (1975*a*), A phase compensation technique for b-mode echoencephalography, *in Ultrasound in Medicine. D. N. White, Ed., New York, NY.: Plenum Press*, 1, 395â404.

Phillips, D., Smith, S., von Ramm, O., Thurstone, F. (1975*b*), Sampled aperture techniques applied to b-mode echoencephalography, *In: Booth N. (eds) Acoustical Holography. Springer, Boston, MA.*, 6, 103–120.

Pinton, G. F., Dahl, J., Rosenzweig, S., Trahey, G. E. (2009), A heterogeneous nonlinear attenuating full- wave model of ultrasound, *IEEE Transactions on Ultrasonics, Ferroelectrics, and Frequency Control*, 56(3), 474–488.

Pinton, G. F., Dahl, J., Trahey, G. (2009), Clutter and sources of image degradation in fundamental and harmonic ultrasound imaging, *in* 2009 IEEE International Ultrasonics Symposium, pp. 2300–2303.

Pinton, G. F., Trahey, G. E., Dahl, J. J. (2011), Sources of image degradation in fundamental and harmonic ultrasound imaging using nonlinear, full-wave simulations, *IEEE transactions on ultrasonics, ferroelectrics, and frequency control*, 58(4), 754–765.

Puls, I., Berg, D., Mäurer, M., Schliesser, M., Hetzel, G., Becker, G. (2000), Transcranial sonography of the brain parenchyma: comparison of b-mode imaging and tissue harmonic imaging, *Ultrasound in Medicine Biology*, 26(2), 189–194.

Rachlin, D. (1990), Direct estimation of aberrating delays in pulse-echo imaging systems, *The Journal of the Acoustical Society of America*, 88(1), 191–198.

Renaud, G., Clouzet, P., Cassereau, D., Talmant, M. (2020), Measuring anisotropy of elastic wave velocity with ultrasound imaging and an autofocus method: application to cortical bone, *Physics in Medicine & Biology*, 65(23), 235016.

Renaud, G., Kruizinga, P., Cassereau, D., Laugier, P. (2018), In vivo ultrasound imaging of the bone cortex, *Physics in Medicine & Biology*, 63(12), 125010.

Rigby, K., Chalek, C., Haider, B., Lewandowski, R., O'Donnell, M., Smith, L., Wildes, D. (2000), Improved in vivo abdominal image quality using real-time estimation and correction of wavefront arrival time errors, *IEEE Ultrasonics Symposium Proceedings*, 2, 1645–1653.

Salles, S., Shepherd, J., Vos, H. J., Renaud, G. (2021), Revealing intraosseous blood flow in the human tibia with ultrasound, *JBMR Plus*, p. e10543.

Sanabria, S. J., Ozkan, E., Rominger, M., Goksel, O. (2018), Spatial domain reconstruction for imaging speed-of-sound with pulse-echo ultrasound: simulation and in vivo study, *Physics in Medicine & Biology*, 63(21), 215015.

Shung, K. (2015), *Diagnostic Ultrasound: Imaging and Blood Flow Measurements - Second Edition*, CRC Press - Taylor & Francis Group.

Smith, S., Trahey, G., Von Ramm, O. (1986), Phased array ultrasound imaging through planar tissue layers, *Ultrasound in medicine & biology*, 12(3), 229–243.

Soulioti, D. E., EspÃndola, D., Dayton, P. A., Pinton, G. F. (2020), Super-resolution imaging through the human skull, *IEEE Transactions on Ultrasonics, Ferroelectrics, and Frequency Control*, 67(1), 25–36.

Spencer, K., Bednarz, J., Rafter, P., Korcarz, C., Lang, R. (1998), Use of harmonic imaging without echocardiographic contrast to improve two-dimensional image quality, *The American Journal of Cardiology*, 82(6), 794–799.

Sumino, Y., Waag, R. C. (1991), Measurements of ultrasonic pulse arrival time differences produced by abdominal wall specimens, *The Journal of the Acoustical Society of America*, 90(6), 2924–2930.

Szabo, T. (2013), *Diagnostic Ultrasound Imaging: Inside Out (2nd Edition)*, Academic Press.

Tanter, M., Thomas, J.-L., Fink, M. (1998), Focusing and steering through absorbing and aberrating layers: Application to ultrasonic propagation through the skull, *The Journal of the Acoustical Society of America*, 103(5), 2403–2410.

Thomsen, L. (1986), Weak elastic anisotropy, *GEOPHYSICS*, 51(10), 1954–1966.

Trahey, G., Freiburger, P., Nock, L., Sullivan, D. (1991), In vivo measurements of ultrasonic beam distortion in the breast, *Ultrasonic Imaging*, 13(1), 71–90.

Trahey, G., Zhao, D., Miglin, J., Smith, S. (1990), Experimental results with a real-time adaptive ultrasonic imaging system for viewing through distorting media, *IEEE Transactions on Ultrasonics, Ferroelectrics, and Frequency Control*, 37(5), 418–427.

Treeby, B. E., Jaros, J., Rendell, A. P., Cox, B. T. (2012), Modeling nonlinear ultrasound propagation in heterogeneous media with power law absorption using a k-space pseudospectral method., *J Acoust Soc Am*, 131(6), 4324–4336.

Treeby, B., Varslot, T., Zhang, E., Laufer, J., Beard, P. (2011), Automatic sound speed selection in photoacoustic image reconstruction using an autofocus approach., *J Biomed Opt*, 16(9), 090501.

Vignon, F., Aubry, J. F., Tanter, M., Margoum, A., Fink, M. (2006), Adaptive focusing for transcranial ultrasound imaging using dual arrays, *The Journal of the Acoustical Society of America*, 120(5), 2737–2745.

Vignon, F., Shi, W., Burcher, M., Powers, J. (2008), Determination of temporal bone isoplanatic patch sizes for transcranial phase aberration correction, *in* 2008 IEEE Ultrasonics Symposium, pp. 1286–1289.

Wiskin, J., Malik, B., Natesan, R., Lenox, M. (2019), Quantitative assessment of breast density using transmission ultrasound tomography, *Med Phys*, 46(6), 2610–2620.

Yoon, H. S., Lawrence Katz, J. (1976), Ultrasonic wave propagation in human cortical boneâii. measurements of elastic properties and microhardness, *Journal of Biomechanics*, 9(7), 459–464.